

Revealing The Dynamics of the Feb 6th 2023
M7.8 Kahramanmaraş/Pazarcik Earthquake:
near-field records and dynamic rupture
modeling

Mohamed Abdelmeguid^{1*†}, Chunhui Zhao^{2†}, Esref
Yalcinkaya³, George Gazetas⁴, Ahmed Elbanna^{2,5*} and Ares
Rosakis^{1*}

^{1*}Graduate Aerospace Laboratories, California Institute of
Technology, 1200 E. California Boulevard , Pasadena, 91125, CA,
USA.

²Department of Civil and Environmental Engineering, University
of Illinois at Urbana Champaign, 205 N. Mathews Avenue,
Urbana, 61801, IL, USA.

³Department of Geophysical Engineering, Istanbul
University-Cerrahpasa, 34320 Avcilar, Istanbul, Türkiye.

⁴Department of Civil Engineering, National Technical University
of Athens, 9, Iroon Polytechniou Str, Athens, Greece.

⁵Beckman Institute of Advanced Science and Technology,
University of Illinois at Urbana Champaign, 405 N. Mathews
Avenue, Urbana, 61801, IL, USA.

*Corresponding author(s). E-mail(s): meguid@caltech.edu;
elbanna2@illinois.edu; arosakis@caltech.edu;
Contributing authors: chunhui3@illinois.edu; eyalcin@iuc.edu.tr;
gazetas@mail.ntua.gr;

†These authors contributed equally to this work.

Abstract

The 2023 M_w 7.8 Kahramanmaraş/Pazarcik earthquake was larger and more destructive than what had been expected. Here we analyzed near-field seismic records and developed a dynamic rupture model that reconciles different currently conflicting inversion results and reveals spatially non-uniform propagation speeds in this earthquake, with predominantly supershear speeds observed along the Narli fault and at the southwest (SW) end of the East Anatolian Fault (EAF). The model highlights the critical role of geometric complexity and heterogeneous frictional conditions in facilitating continued propagation and influencing rupture speed. We also constrained the conditions that allowed for the rupture to jump from the Narli fault to EAF and to generate the delayed backpropagating rupture towards the SW. Our findings have important implications for understanding earthquake hazard and guiding future response efforts and demonstrates the value of physics-based dynamic modeling fused with near-field data in enhancing our understanding of earthquake mechanisms and improving risk assessment.

Keywords: Episodic Supershear, Kahramanmaraş/Pazarcik Earthquake, Supershear Ruptures, Near Fault Strong Motion Records

Introduction

On February 6th 2023, a M_w 7.8 earthquake, currently known as the Kahramanmaraş/Pazarcik earthquake, shook the southeastern parts of Türkiye and northern Syria. Preliminary back projection models based on teleseismic data as well as multiple seismic inversions suggest that the rupture initiated at 1:17:35.5 coordinated universal time (UTC) on a splay fault (the Narli fault) in the near proximity of the East Anatolian fault [1, 2]. The hypocenter location is estimated by USGS to be 37.230°N 37.019°E with a depth of approximately 10 km [1, 2]. The rupture then propagated north east subsequently transferring to the East Anatolian fault and starting a sequence of seismic events. Furthermore, subsequent preliminary geodetic inversions confirmed the multi-segment nature of the M_w 7.8 rupture. The sequence of events resulted in catastrophic levels of destruction with substantial humanitarian and financial losses[3].

The M_w 7.8 Kahramanmaraş/Pazarcik earthquake was, by many measures, bigger and more destructive than what had been expected based on historical records in the past several centuries[4]. The estimated magnitude of the largest earthquake that occurred on the East Anatolian Fault (EAF) in the last few hundred years is 7.2 which is believed to be either the 1789 Palu (Elazığ) earthquake or the 1872 Amanos earthquake[5, 6]. This estimate is smaller than the magnitude of the Kahramanmaraş/Pazarcik earthquake. Furthermore, each of these historic events ruptured a segment of the EAF but none was extended over multiple segments as the recent event.

From a geological point of view, there are several features associated with the fault system that could have contributed to the extent of damage associated with the M_w 7.8 Kahramanmaraş/Pazarcik earthquake. Studies of the tectonic setting suggest that the orientation of the EAF with respect to the principal stresses places several fault segments within a highly stressed regime that is sensitive to minor perturbations associated with dynamic stress transfer and dynamic stress rotations. Furthermore, the fault network is geometrically complex with multiple fault segmentations, kinks, and bends which strongly influences the dynamics of rupture propagation [7–11]. The existence of geometrical complexity within this high stress regime could further amplify its role on rupture dynamics through, for example, the emergence of regions with high stress concentrations, generation of arrest phases, back propagation of earthquake rupture, or development of episodes of transient supershear propagation.

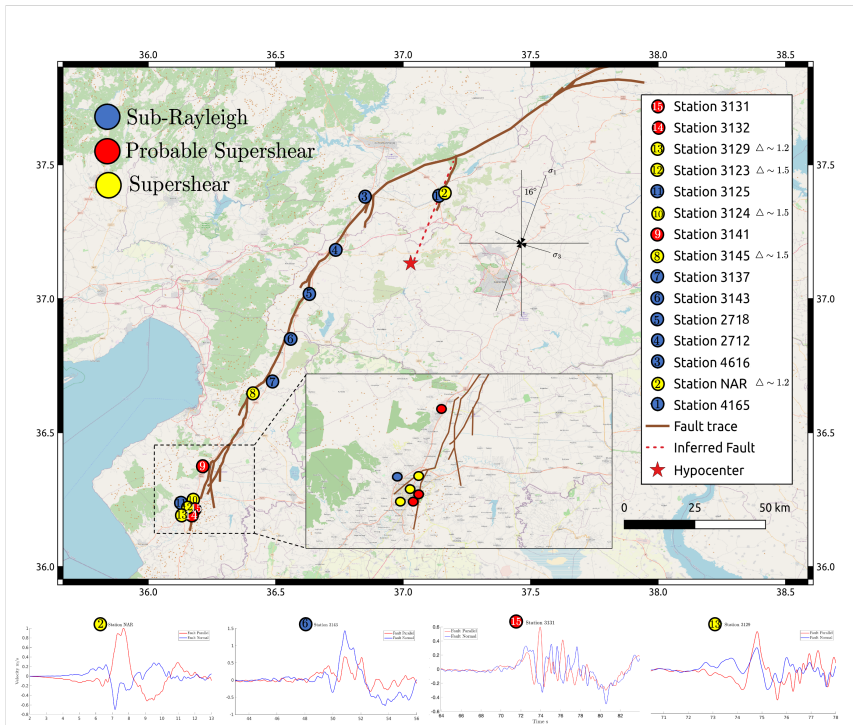
Preliminary analysis of the Kahramanmaraş/Pazarcik earthquake based on the dense network of ground motion stations deployed by AFAD revealed that the rupture that initiated on the Narli fault has transitioned to supershear speeds prior to eventually triggering the EAF [12]. This initial rupture propagated along the splay fault at sub-Rayleigh speeds for approximately 19 km prior to transitioning to a supershear event for the remaining length of the Narli fault before reaching the EAF [12]. Supershear ruptures generate largely unattenuated shock waves [13], are more efficient in dynamic triggering [14], and are thus likely to contribute to the migration of the rupture to EAF. However, It remains to be investigated whether the supershear nature of the incoming rupture is a sufficient condition for such triggering to occur.

The propagation speed of the rupture along the EAF is currently being debated with competing views. On one hand, through joint kinematic inversion of HR-GNSS and the ground motion data, Melgar et al 2023 suggested that the most likely estimate of the rupture speed on the EAF is 3.2 km/s for the M_w 7.8 earthquake [15]. This conclusion is based on an average propagation speed during the entire event sequence which is most unlikely to be representative of such a complex fault network with multiple kinks and branches which result in unsteady, and intermittent rupture propagation [16, 17]. On the other hand, Okuwaki et al 2023 using potency-density tensor inversion suggests that the rupture propagation for M_w 7.8 earthquake involves discrete segmented supershear propagation along certain fault segments [18].

These contradicting messages regarding the rupture propagation speed, along with Gazetas' work showing abnormally high ground velocities and acceleration in near fault records near Antakya (G. Gazetas, personal communication, February 20, 2023), prompted us to investigate the possibility of transient supershear ruptures beyond those observed at the triggering of M_w 7.8 earthquake [12]. To that end, we first utilize the dense seismic network provided by AFAD to study the ground motion records of stations located in near proximity of the fault trace. Through mechanistic understanding of the characteristic features associated with supershear rupture we identify locations

4 *The Dynamics of the M_w 7.8 Kahramanmaraş Türkiye Earthquake*

139 which demonstrate supershear speeds. We then build a 2D dynamic rupture
 140 model of the Kahramanmaraş/Pazarcik earthquake based on constraints from
 141 the ground motion records, field studies of the tectonic setting, and geometric
 142 features of the fault trace. Through this two-fold approach we provide phys-
 143 ical arguments to better constrain the rupture velocity profile for competing
 144 earthquake kinematic inversions, and provide insight on the mechanisms that
 145 contributed to such devastation and humanitarian loss.

147 **Station Analysis**

173 **Fig. 1** A Map of the East Anatolian Fault (EAF) zone highlighting the
 174 **estimated location of the hypocenter of the M_w 7.8 Kahramanmaraş/Pazarcik**
 175 **earthquake.** : The location of seismic monitoring stations are highlighted by circular
 176 shapes within the map. Stations are distinguished by their colors indicating a ground record
 177 characteristic consistent with sub-Rayleigh (blue), a supershear rupture (yellow), and prob-
 178 able supershear (red). For stations that demonstrate supershear characteristics we indicate
 179 the ratio of fault parallel to fault normal component within the label. (b-e) Examples of
 180 the instrument corrected ground motion records filtered at 2 seconds for multiple stations
 181 highlighting each rupture speed scenario. Inserts to the figure shows a zoomed view of the
 182 stations located at the southern end of the fault trace. The direction of the principal stress
 183 obtained from prior field assessment is highlighted on the map.

Figure 1 illustrates a detailed mapping of the fault trace obtained from USGS. It also includes the estimated location of the hypocenter according to USGS [1], marked by the red star, and the location of multiple seismic stations deployed by AFAD [2]. Several of these stations are located very close to the fault surface and thus provide detailed insight into the near-field characteristics of the fault rupture. For example, Rosakis et al. 2023 used the stations across the Narli splay fault, labeled on the map with a blue circle 1(4165) and a green circle 2 (NAR), to show that the rupture went through a transition from sub-Rayleigh to supershear speeds at an epicentral distance of about 19 km [12]. Similar to Rosakis et al 2023, we investigate the ground motion velocity records along the fault parallel, the fault normal directions but expand our analysis here to include all the near-field stations with complete and reliable records. The raw NS, EW and vertical acceleration records are obtained from (AFAD : Disaster and Emergency Management Authority) and (KOERI : Kandilli Observatory and Earthquake Research Institute) respectively (Retrieved 02/09 5:18 PST) [2, 19].

As discussed in Rosakis et al 2023 and Mello et al 2014, a major characteristic of supershear ruptures [20, 21] is a dominant fault parallel ground velocity component relative to the fault normal one [22, 23]. Accordingly, we classify the stations based on the ratio of the fault parallel $\delta\dot{u}_{FP}^s$ to the fault normal component $\delta\dot{u}_{FN}^s$ into three main categories: (1) a sub-Rayleigh station is one which experiences a dominant fault normal component, (2) a potentially supershear station is one in which the FP component is comparable to the FN component, and (3) a supershear station is one in which the FP clearly dominates the FN velocity. In the legend, we provide the complete list of the stations alongside with the value of the ratio of the FP to FN components of the ground velocity when it represents a supershear case. This analysis allows us to identify regions along the fault where we suspect a supershear rupture has propagated during the M_w 7.8 earthquake. Figure 1b-e provides examples of the ground motion records for each rupture scenario. All the records for the other stations are included in the Appendix Figure A1.

The ground motion records reveal three locations in which the rupture propagation speed exceeded C_s . The first incident, discovered in Rosakis et al 2023, occurs along the splay fault (the Narli fault) in very close proximity to the hypocentral location [12]. After transitioning to the EAF, the rupture propagated bilaterally. One tip propagated in the NNE direction towards Malatya while the other tip propagated in the SSW direction towards Antakya. Several stations exist along the latter segment and provide sparse but important constraints on the rupture speed in that direction. Specifically, the records at stations 4 (2712), 6 (3143), and 7 (3137) show larger FN ground velocity components compared to the FP component suggesting sub-Rayleigh propagation speed along this major segment of the EAF. Station 8 (3145) shows an opposite signature indicated by the dominant FP component in the ground velocity record. The ratio of the FP to FN components at this station is approximately 1.5 suggesting that the rupture is propagating at a supershear speed. In Figure

1, station 9(3141) is located along a segment of the EAF with a strike of 55° which varies from the average segment strike of 25° , indicating that the sudden change in the fault strike and the resulting change in the local stress state is favorable, and could have contributed, to the transition to a supershear rupture. Finally, we observe that the rupture transitioned again to supershear near the end of the fault trace as indicated by the multitude of stations (10-15) located in Hatay province. Except for station 11 (3125), the other records indicate a more dominant FP to FN component ratio. However, the ratio varies between stations. This maybe explained by the complexity of the fault network within this region. The multiple kinks and branching segments in the southern tip suggest a complex stress state that contributes to bursts of supershear on some segments and complex waveform that may obscure the Mach cone signature in other locations. It also contributes to a stress shadowing effect on some other segments that may slow down the rupture or even prevent it from further propagation as it might have been the case for the branch near station 11 (3125).

Our analysis of the near-field station records suggests that the rupture propagation over the Narli fault as well as the SSW segment of the EAF has been with a mix of sub-Rayleigh and supershear speeds. Due to the sparsity of stations around the junction point of the Narli fault with the EAF, as well as along the NNE segment of the EAF, we do not have enough information to constrain the propagation speed along these segments. To fill this gap, we start by developing a mechanistic model for the Narli/EAF junction consistent with the existing records on the Narli fault as outlined in the next sections.

The Narli/EAF Junction model

In order to better constrain the model along regions with minimal station deployment we first construct a minimalistic model of the junction between the Narli fault and the EAF. This simplified model consists of the Narli splay fault and a small portion of the EAF with the objective of obtaining better insights into the rupture migration. Figure 2a shows the region of interest and highlights the sudden change in strike at the intersection. It further shows the simplified fault geometry in this analysis in which both fault strikes are aligned with the inferred estimates provided by USGS [1] which approximate the actual strike based on aftershock records and the complex fault trace shown in Figure 2a.

In our model we adopt a linear slip weakening friction law. Fault slip starts at a point when the shear stress reaches the static shear strength level, given by the product of the static friction coefficient μ_s and the fault normal compressive stress. The stress then decreases linearly with increasing slip δ , over a characteristic slip-weakening distance D_c , to the dynamic shear strength, set by the product of the constant dynamic friction coefficient μ_d and the fault normal compressive stress σ_o .

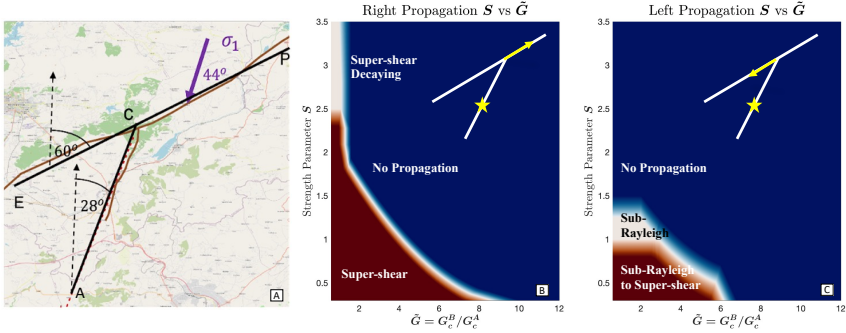


Fig. 2 Geometry and Phase Diagram (strength parameter S and ratio of fracture energies \tilde{G} between main fault and splay fault) of the Junction Model. (a) The idealized geometry of splay fault (AC) and main fault (ECP) with its angle measured with respect to the north direction. Purple arrow represents the direction of maximum principal stress. (b) Phase diagram of right propagation (C to P direction). There are three phases: supershear propagation, supershear propagation with decaying velocity, or no propagation. (c) Phase diagram of left propagation (C to E direction). There are three phases: sub-Rayleigh propagation with transition to supershear after a certain distance, sub-Rayleigh propagation, or no propagation.

To constrain the model, first we consider the tectonic stress state in the region. Prior studies suggest that the angle of maximum compressive stress is in a N16.4°E compression regime (σ_1) [24]. Based on this maximum horizontal stress direction, we show in the Appendix Figure B2, that the ratio of the resolved shear stress to the normal stress on any fault segment is particularly sensitive to the choice of relative principal stresses magnitudes. For example, using the strike of the splay fault and the orientation of the maximum compressive stress, it is apparent from the analysis in the Appendix Figure B2 that any stress ratio σ_1/σ_3 less than 3 would result in a low apparent friction $\mu = \tau/\sigma_o$ (≤ 0.3) on the splay fault. That is probably inconsistent with triggering on an immature, previously unmapped, fault like the Narli fault, and it may hinder the rupture continuation on the EAF assuming reasonable values for the static and dynamic friction coefficients [25, 26]. Specifically, with low apparent friction, the dynamic stress drop may be too low to enable the continued propagation past the junction. However, a stress ratio σ_1/σ_3 of 4 or more would increase the apparent friction to at least 0.5. This overcomes the aforementioned limitations.

Another unique constraint on the model, identified in Rosakis et al 2023, is that the rupture transitioned to supershear on the splay fault after propagating for approximately 19.5 km at sub-Rayleigh speed. The transition to supershear depends on the frictional length scale L_f [27, 28] and the strength parameter S . The strength parameter measures how close the initial stress is to the static strength $S = \frac{\mu_s - \mu}{\mu - \mu_d}$ [20, 29, 30]. The lower S value promotes a fast transition to a supershear wave, whereas the higher value indicates a favorable condition for sub-Rayleigh wave propagation [31]. Here we assume a frictional length scale $L_f = GD_c/\sigma_o(\mu_s - \mu_d) = 1600$ m (G is the shear modulus), which is consistent

277
278
279
280
281
282
283
284
285
286
287
288
289
290
291
292
293
294
295
296
297
298
299
300
301
302
303
304
305
306
307
308
309
310
311
312
313
314
315
316
317
318
319
320
321
322

323 with what is typically inferred for large crustal earthquakes [32]. We further
 324 assume that the static friction coefficient is $\mu_s = 0.7$ which is consistent with
 325 Byerlee's law [33]. To constrain the dynamic friction coefficient, we use a trial
 326 and error approach to obtain a value for S that would yield a transition length
 327 of approximately 19.5 km. We identify this value of S to be $= 0.75$. This low S
 328 value is consistent with the rapid transition to supershear propagation that is
 329 inferred from near field observation. From the known S value, we then obtain
 330 the dynamic coefficient friction for the splay fault as 0.327.

331 Finally, given the above parameters, we adjust the value of the principal
 332 stresses to numerically produce a reasonable value of stress drop which results
 333 in a slip distribution on the splay fault that is consistent with the inferred
 334 slip from the seismic inversion ($\sim 1 - 3$ m). This corresponds to a reasonable
 335 minimum principal stress of $\sigma_3 = -15$ MPa and a maximum principal stress
 336 of $\sigma_1 = -60$ MPa [34] According to this estimate, the average slip on the splay
 337 fault is around 2.0 m and the stress drop is 3.61 MPa. Given these parameter
 338 choices the resulting characteristic length D_c corresponds to $= 0.316$ m. This
 339 completes the choice of parameters for the splay fault, resulting in an inferred
 340 fracture energy $G_c = 1/2\sigma(\mu_s - \mu_d)D_c = 0.998$ MJ/m².

341 To investigate the implications of the constrained splay fault dynamics on
 342 the continued propagation along the EAF, we consider a parametric study of
 343 the junction region. The objective is to constrain the frictional parameters on
 344 EAF and the properties corresponding to an early bilateral propagation beyond
 345 the junction point. To this end, we introduce a dimensionless parameter \tilde{G}
 346 which is defined as G_c^B/G_c^A and correlates with the probability for continuous
 347 propagation after the jump between faults. If one considers a rupture transition
 348 from fault A to fault B, the parameter \tilde{G} measures the relative value
 349 of the fracture energy of fault B to the fracture energy of fault A. This quantity
 350 depends on the frictional parameters and the normal stress resolved along
 351 each individual fault. Theoretically, a small value of the \tilde{G} suggests a favorable
 352 continuous propagation due to comparable fracture energy between fault A
 353 and fault B while a large value of the \tilde{G} suggests unfavorable continued propagation.
 354 In the context of the junction, all the parameters for the splay fault
 355 (fault A) are known quantities and have been constrained using the above procedure.
 356 The objective here is to investigate the space of S and \tilde{G} parameters
 357 for fault B (Line ECP) that would affect both right propagation (From C to
 358 P) and left propagation (From C to E) of the rupture on the EAF (fault B).

359 To conduct this investigation we perform multiple numerical simulations
 360 modeling the rupture transition from fault A to fault B covering a wide
 361 spectrum of frictional parameters. Each individual simulation corresponds to
 362 specific choice \tilde{G} and S on the EAF. In each of these simulations the rupture
 363 on fault A was considered to be supershear as consistent with our previous
 364 discussion. Figure 2b shows the phase plot for the forward propagating front
 365 for a wide range of \tilde{G} and S values. We notice that for every value of S there
 366 is a critical value of \tilde{G} such that there is no propagation to the right of the
 367 junction. The relationship between that critical value of \tilde{G} and S is given
 368

graphically by the boundary between the blue and the white/brown regions. We observe that as S decreases the critical value of \tilde{G} required for continuous propagation increases. This can be intuitively understood as a competition between required fracture energy and fault strength, namely as the fracture energy increases, the initial traction needs to be closer to the static strength to allow for continuous propagation. However, for values of \tilde{G} that permits the continued propagation, we observe that the rupture propagates as a sustained supershear if S is small enough (brown region) and as a decaying supershear if S is sufficiently large ($S > 2.5$) (white region). It is obvious from Figure 2b that if there is rupture propagation to the right then this rupture has to initiate as a supershear rupture regardless of the choice of the parameters. This is consistent with the experimental analysis conducted by Rousseau and Rosakis 2003 which investigated the rupture propagation speed for a crack encountering a branch[35]. The study of Rousseau and Rosakis evaluated a wide spectrum of branch angles, and showed that for acute branching angles (similar to the angle between the splay fault and EAF) the crack speed along the branch would initially be the same or slightly smaller than its propagation speed prior to encountering the branch[35, 36].

Figure 2c shows the characteristics of the left propagating rupture in terms of the \tilde{G} and S parameters. We observe that should $S > 1.5$, regardless of the \tilde{G} parameter, no back propagation will be observed. We note that $S > 1.5$ would still allow propagation to the right should \tilde{G} be small enough. Inversely, if $S < 0.9$ the rupture will back propagate initially as sub-Rayleigh prior to transitioning to supershear with the critical value of \tilde{G} increasing as S decreases. For intermediate choices of S ($0.9 < S < 1.5$), if \tilde{G} is small enough, the rupture can back propagate at sub-Rayleigh speeds or not propagate in the backward direction at all for higher values of \tilde{G} . Seismic inversions reveal that there is indeed a backward propagating rupture. To further reconcile the findings for both the right and left propagation, and assuming that the frictional properties on both segments are the same, we may conclude that $S < 1.5$ and a small enough \tilde{G} , would satisfy both conditions of backward propagation and sustained supershear rupture for the forward propagation.

Within the limitations of our linear elastic model that assumes uniform initial stress and frictional properties on the EAF segment at the junction, the parametric study above reveals several important findings which we summarize as follows. (1) The continuous propagation of the rupture to the right is conditional on a critical value of \tilde{G} which depends on S . (2) Should the supershear rupture successfully jump from the splay fault to the main fault, the rupture propagation to the right has to start as a supershear. (3) The continued propagation to the right of the junction is a necessary but not a sufficient condition for the triggering of the rupture propagation to the left. This back propagating rupture additionally requires a relatively low S value ($S < 1.5$). (4) If S is too low ($S < 0.9$), the back propagating rupture could eventually

369
370
371
372
373
374
375
376
377
378
379
380
381
382
383
384
385
386
387
388
389
390
391
392
393
394
395
396
397
398
399
400
401
402
403
404
405
406
407
408
409
410
411
412
413
414

415 transition into supershear. This highlights the critical dynamics of the junc-
 416 tion and the sensitive dependence of the details of the rupture propagation on
 417 the stress and frictional parameters.

418

419 **2D Dynamic Rupture Model Setup**

420

421 After constraining the conditions that allow the bilateral propagation of the
 422 rupture on the EAF after jumping from the Narli fault, our next step is to
 423 characterize the rupture propagation along the multiple major fault segments.
 424 To that end, we consider a 2D model of a non-planar branching fault network
 425 of strike slip faults utilizing the estimated fault trace provided by USGS based
 426 on fault offsets [1]. We start by generating a smoother version of the fault
 427 trace by adopting the estimated strikes of the three major segments from the
 428 USGS finite fault model for the M7.8 Kahramanmaraş/Pazarcik earthquake
 429 [1]. We then enrich the model at specific locations by incorporating confirmed
 430 branches and kinks. As shown in Figure 3 the fault model consists of three
 431 primary segments spanning the two strike slip faults: the first segment, AC,
 432 represents the Narli fault (the splay fault that hosted the hypocenter and the
 433 initial rupture propagation). The second and third segments, segments EW
 434 and ET, are both part of the EAF with different overall strike angles consistent
 435 with the USGS model. We extend our model to capture the complexity in the
 436 fault network within the southern part between nodes H and T by incorporat-
 437 ing multiple branches and changes in the strike. We have expanded the model
 438 in the NNE direction by adding segment WX consistent with the mapped fault
 439 trace. We have also added two major branches, segments PV and FG, that are
 440 also confirmed by USGS mapping. Furthermore, since the EAF is a relatively
 441 young fault and is a highly disordered one [37–39], we assume the fault seg-
 442 ments are discontinuous at the locations of different geometric complexities,
 443 such as kinks and junctions between different intersecting faults. We highlight
 444 these locations with blue filled dots in Figure 3. Introduction of this strong
 445 segmentation may lead to transient rupture propagation interruption. How-
 446 ever, this would still be consistent with what is expected on a geometrically
 447 complex fault system with multiple kinks, branches, and changes in strike as
 448 the one studied here.

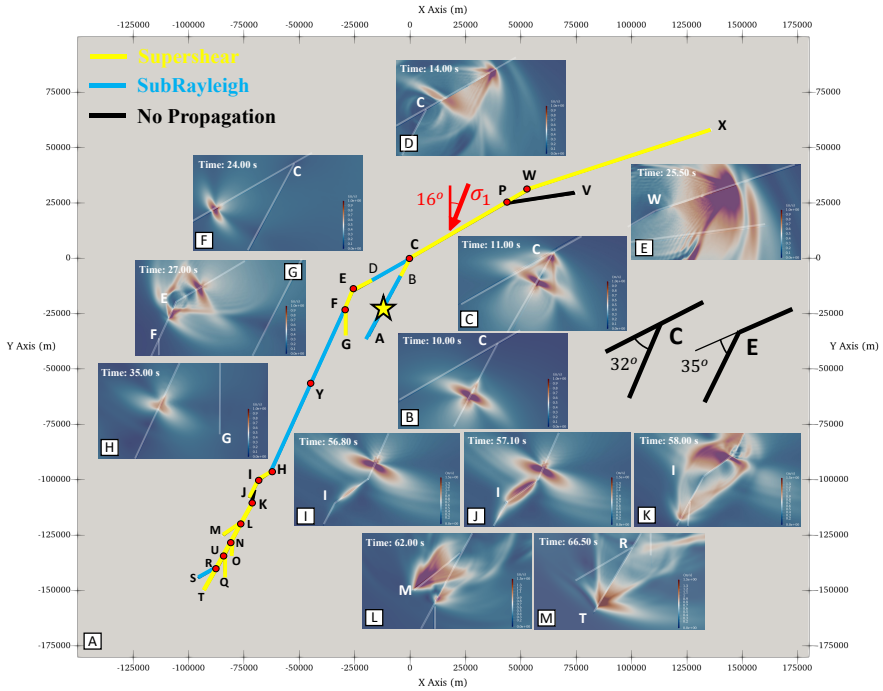
449 With the frictional parameters constrained on the splay fault at hand,
 450 together with the findings after conducting the \tilde{G} - S parametric study in the
 451 previous section, we proceed to construct the appropriate frictional parameters
 452 for the other fault segments as follows: First, we assume that the static friction
 453 coefficient is constant for all fault segments and we set it to be $\mu_s = 0.7$.
 454 This choice is within the reasonable range for the static friction coefficients
 455 according to Byerlee’s law[33]. As the rupture jumps onto the main fault (Line
 456 EW) , we choose $S = 0.9$ and $\tilde{G} = 1.155$ so that we can ensure bilateral
 457 propagation beyond the junction point C. This choice of the S parameter
 458 allows supershear rupture to the north east (right) and sub-Rayleigh rupture,
 459 which potentially transitions into supershear, to the south west (left). Given
 460

an apparent friction $\mu = 0.612$, this sets the dynamic friction to $\mu_d = 0.515$. The lower value of \tilde{G} promotes the continuous bilateral propagation along the main fault. For the fault beyond the left kink (Line EH), S is assumed to be 2.0 so that sub-Rayleigh rupture is more favorable, which agrees with the signals received by the near-field stations (Figure 1 Stations 3,4,5). As for the dynamic friction parameter, all faults beyond the left kink (Point E) have a dynamic friction coefficient of 0.26. This ensures that $\mu_d < \mu$ so the dynamic propagation is facilitated by a positive dynamic stress drop. It also ensures that the parameter \tilde{G} is low enough to make it possible for the rupture to navigate the changes in strike and potentially trigger the branched segments in the southern region. Due to their orientation with respect to the background stress field, the faults located in the south end are highly stressed. With the choice of the frictional parameters outlined above, these faults ended up having a small S values (~ 0.4) which makes supershear likely.

Results

Figure 3 illustrates velocity magnitude snapshots of the rupture propagation at different time steps alongside a sketch of the fault system. The figure also shows the direction of the maximum horizontal principal stress, label the points of interest alphabetically, sketch the angles at kink C and kink E and mark each discontinuous junction point with a blue dot. We have also assigned different colors to mark different fault segments according to their rupture propagation speeds as will become apparent from the subsequent discussion. The rupture is first nucleated by overstressing on the splay fault (Segment AC) with the epicenter ~ 30 km from the junction (Point C). The initial rupture propagates bilaterally with sub-Rayleigh speed, The rupture tip heading south arrests at the end of the splay fault (Point A). The rupture heading toward the EAF transitions to supershear speed after ~ 20 km of sub-Rayleigh propagation (Point B, Figure 3b). The supershear nature of the transitioned rupture is confirmed by the near-field stations (NAR), and is reproduced here with the clearly visible Mach cone in (Figure 3b-c). As the rupture jumps onto the main fault (Line EW, Figure 3c), the rupture to the north east (right) continues with the supershear speed (Figure 3d) and eventually jumps into the kink point (Point W) (Line WX, Figure 3e).

A delayed rupture to the south west (left) initiates at the junction Point C at around ~ 20 s, and propagates along segment CE. This time roughly agrees with the inferences based on seismic inversions [15]. This left going rupture initially propagates with sub-Rayleigh speed (along CD) (Figure 3f) and eventually transitions into supershear speed (Point D) just before jumping over the left kink (Point E, Figure 3g). The supershear rupture then gets frustrated and transitions to sub-Rayleigh after hitting the junction at the fork (Point F). The resulting sub-Rayleigh rupture continues propagating along the straight FH segment towards point H, until it reaches the region of increased geometrical complexity at the south end of the EAF. As the sub-Rayleigh



529 **Fig. 3** Idealized fault geometry and velocity magnitude Snapshots at specific
 530 locations along the rupture path. Red arrow represents the direction of maximum
 531 principal stress σ_1 , the yellow star is where the epicenter is located. Along the fault trace,
 532 each junction point is labeled alphabetically, where the blue dots indicate the discontinuity.
 533 Segment angles associated with junctions C and E are given. Yellow color, blue color and
 534 black color represent fault traces showing supershear, sub-Rayleigh and no propagation
 535 respectively.

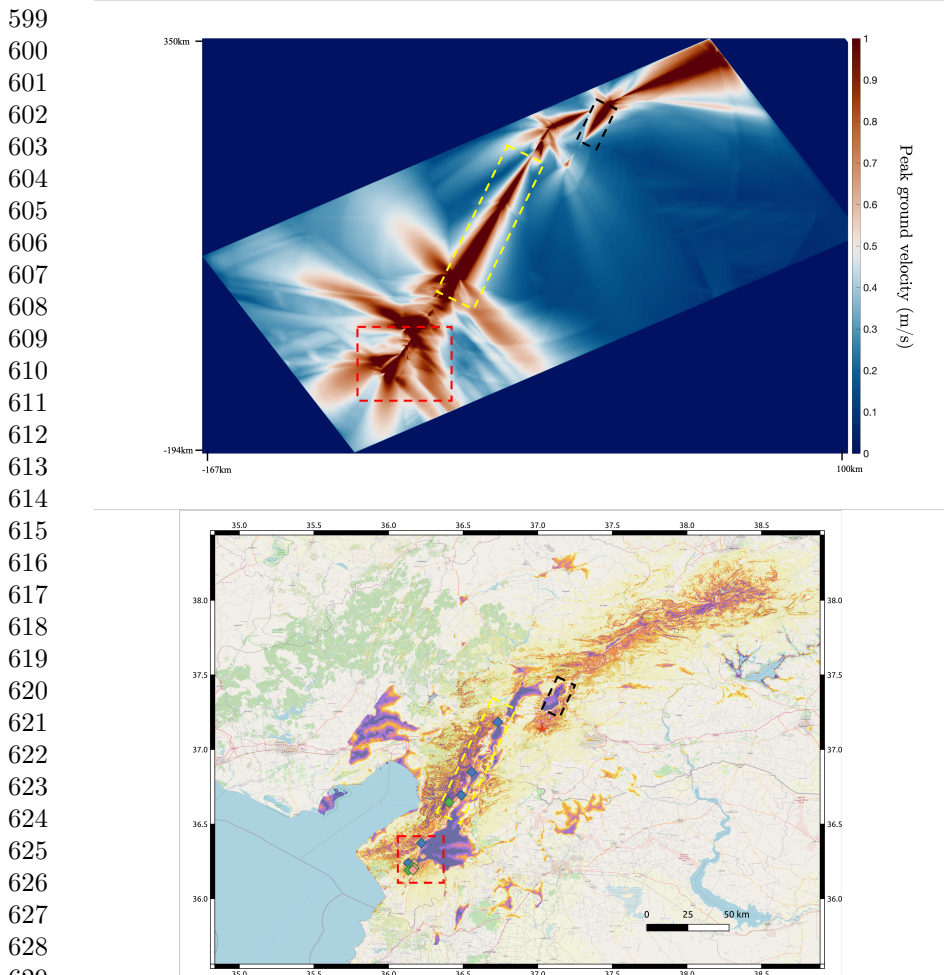
536 rupture approaches the end of the fault segment FH it remotely triggers a
 537 supershear rupture near Point I due to the wave field associated with incoming
 538 rupture. This supershear propagates backwards along segment IH towards
 539 Point H and merges with the incoming sub-Rayleigh rupture, (See Figure 3i-j).
 540 The surprising behavior captured by the model agrees with the adjacent near
 541 field records showing that the station close to Point I (Appendix Figure A1f)
 542 receives the rupture signal ~ 0.5 seconds earlier than the station close to Point
 543 H (Appendix Figure A1e). At the same time, the same rupture propagates at
 544 supershear speed along branch IJ prior to arresting at J (See Figure 3k). As
 545 the radiated waves from the arrested phase propagates towards the southern
 546 end, a new rupture is remotely triggered along segment KT near point K by
 547 the dynamic stress field. This rupture rapidly transitions to supershear as it
 548 continues to travel along the main fault segment KT while simultaneously acti-
 549 vating supershear ruptures along the neighboring branches (for example Point
 550 M, Figure 3l). This main rupture continues to propagate as supershear until
 551 it reaches the end of the fault at Point T (Figure 3m). As shown in Figure
 552 1, there is a cluster of stations in this region that receives supershear signals.

The fortuitous existence of a cluster of stations near the end of the fault trace, many of which record the characteristic signatures of supershear propagation, verifies the model predictions of supershear propagation near Hatay.

Our dynamic rupture model captures the following key features of the M_w 7.8 complex event. (1) The initial nucleation of the rupture along the Narli fault and its transition to supershear at ~ 19.5 km away from the hypocenter. (2) The subsequent triggering of the EAF by the incoming supershear rupture. (3) The bilateral (NEE and SSW) propagation along EAF with a mix of sub-Rayleigh and supershear speeds. (4) A long portion of sub-Rayleigh growth along a major SSE segment of the EAF. (5) The sustained supershear growth and eventual arrest of the rupture at the southernmost end of the fault trace near Hatay. Finally, the model shows that the geometric complexity and the highly heterogeneous stress field contributed to this mix of rupture speeds along different segments, as well as, additional bursts of supershear propagation along the various branches of the EAF.

Figure 4a shows peak ground velocity contours for the duration of the simulated earthquake event obtained from the dynamic rupture model. We observe regions of intense ground velocity associated with the rupture propagation (highlighted by dashed squares). The width and extent of the intense ground motion depends on multiple factors such as the rupture propagation speed, geometrical complexity, and local frictional parameters. As highlighted earlier, the characteristics of the ground motion vary based on whether the rupture is propagating at supershear or sub-Rayleigh speeds. The intensity of the ground shaking would also depend on the stress drop which is influenced by the frictional parameters. The triggering and path selection along a complex fault network during the earthquake would play a significant role in the distribution of PGV (peak ground velocity) within the domain. Furthermore, in the dynamic rupture model, we also observe high intensity, widely distributed ground motion near geometrical features such as the junction between the splay fault and the EAF, as well as around the left kink (Point E).

To associate the ground failure estimates in the M_w 7.8 Kahramanmaraş/Pazarcik earthquake with the ground motion records obtained from the numerical model, Figure 4b shows a map of the modeled region. On this map, we superimpose the predictions of the ground failure models generated by USGS, mainly the landslide and liquefaction estimates[1]. Both ground failure models are based on analysis of historic records of liquefaction and landslides of seismically induced ground failure. The landslide distribution models are generated based on the spatially distributed estimates of ground velocity shaking (PGV), topographic slope, lithology, land cover type, and a topographic index designed to estimate variability in soil wetness. The landslide distribution models estimated by USGS are consistent with the mapped coseismic landslides by the landslide assessment team of the 2023 Türkiye earthquake sequence (SLATE). The liquefaction model is based on slope-derived VS30, modeled water table depth, distance to coast, distance to river, distance to the closest water body, and precipitation and peak ground velocity (PGV).



630 **Fig. 4 Correlation of ground shaking with ground failure estimates.** (a) Peak
631 ground velocity (PGV) distribution obtained from the numerical simulation of dynamic
632 rupture. The peak velocity distribution demonstrates regions of large magnitude PGV dis-
633 tribution. Geometrical complexity, triggering of segmented faults and largely unattenuated
634 shock fronts due to supershear propagation contributes toward a wider distribution of ground
635 shaking. (b) Ground failure estimates from USGS showing probability of liquefaction and
636 landslide. The more extensive ground failure correlates with regions of wider and more
637 intense ground shaking observed in our numerical model. We note that field reconnaissance
638 of ground failure shows agreement with USGS predictions.

638 The liquefaction estimates from the USGS model agree with the preliminary
639 mapping of liquefaction sites based on remote sensing data [40].

640 Based on both preliminary reporting and USGS estimates of ground failure
641 we observe that regions with more distributed (mildly attenuated with distance
642 from the fault) and intense ground motion obtained from the dynamic rupture
643 model are consistent with regions of substantially larger destruction. Of course,
644

the nature of the failure may be influenced by phenomena such as soil and basin amplification, in addition of course to the type and quality of construction. Supershear ruptures with intense ground motion and largely unattenuated shock fronts would probably amplify the extent and magnitude of damages associated with either structure or ground failures. Specifically, we observe that the peak slip rate rapidly change over short distances in regions of supershear propagation to south (Appendix Figure E4). This non-steady supershear propagation, increases the intensity of shaking and enhances the radiated energy. Furthermore, we observe that the ground motion records show a relatively narrow (1-2 seconds) dominant pulse in regions with supershear propagation such as observed in Antakya (Appendix Figure A1j,k) compared to records corresponding to sub-Rayleigh propagation (Appendix Figure A1d,e,i). The presence of a relatively narrow velocity pulse imposes higher demand on the structures, increasing the possibility of structural collapse.

Specifically, in the dynamic rupture model, we observe supershear propagation at the southern end of the fault segment in the region of Hatay near Antakya, resulting in high particle velocity magnitude (~ 2 m/s) and widespread ground shaking (red dashed box). Simultaneously, the records highlight significant ground failure associated with both liquefaction and coseismic landslides within the same region. A similar pattern is also observed in NNE directions toward Malatya where we may correlate the supershear propagation in that direction with the estimates of widespread landslides in the region. Furthermore, the predicted liquefaction zone around the northern end of the Narli fault (black dashed box) also seems to correlate well with the region of supershear transition and propagation on that segment.

Discussion

Our analysis of near-field records of the $M_{7.8}$ Kahramanmaraş/Pazarcik earthquake reveals that the rupture propagation speed was spatially not uniform; rather it varied from sub-Rayleigh to supershear speeds at different sections. This is consistent with several experimental studies and numerical simulations of geometrically complex faults which demonstrated that the existence of kinks and branches may have significant implications on the rupture terminal speed depending on the geometrical setup in relation to the orientation of the principal stresses [35, 41, 42]. According to the near-field records, supershear speeds are observed predominantly along the splay fault (Narli fault) that hosted the initial rupture, and at the SSW end of the fault trace within the Hatay region. Furthermore, the geometrical complexity of the fault contributed to the emergence of transient supershear ruptures as revealed by the ground motion records showing dominant fault parallel components along fault segments with steep strike changes relative to the backbone strike. These findings reconcile the currently available seismic inversions that arrived at contradictory conclusions regarding the rupture speed.

645
646
647
648
649
650
651
652
653
654
655
656
657
658
659
660
661
662
663
664
665
666
667
668
669
670
671
672
673
674
675
676
677
678
679
680
681
682
683
684
685
686
687
688
689
690

691 The dynamic rupture model for the junction region between the Narli fault
692 and the EAF allowed us to identify a regime of frictional parameters, and
693 infer physical constraints that would be consistent with sustained propagation
694 along both the NE and SW directions of the EAF. We find that sustained
695 propagation in the NE direction of EAF necessitates that the rupture initially
696 propagates to the north at supershear speeds. We have also found that the con-
697 tinued rupture propagation to the NE is necessary but not sufficient to trigger
698 a delayed nucleation of the left propagating rupture towards SE. The strength
699 parameter to the SW side of the junction must also be low enough to enable
700 the nucleation and propagation of the left propagating rupture. Furthermore,
701 a combination of high dynamic stress drop on the Narli fault and high stresses
702 on the EAF appear to have been necessary to facilitate the rupture jumping
703 across the two faults.

704 Our dynamic rupture model further highlights the effect of geometrical
705 complexity on the rupture propagation speed and rupture physics. Through
706 incorporating the geometrical complexity at the intersection between the Narli
707 fault and EAF we reproduce a major feature of this earthquake, which is the
708 emergence of a delayed back propagation ~ 20 secs to the left of the junction
709 point. While initially the angle to the left is unfavorable to sustain a rup-
710 ture propagation, the growth of the stress concentration, due to the dynamic
711 stress transfer and continued rupture propagation towards the NNE, eventu-
712 ally overcomes the static strength of the left side of the junction, which has
713 been lowered due to a tensile stress perturbation imparted by the incoming
714 rupture on the Narli fault. The combination of these factors led to a delayed
715 nucleation and subsequent propagation in the SSW direction. Although the
716 incoming rupture from the Narli fault was supershear, this delayed propaga-
717 tion initiated as a sub-Rayleigh crack prior to transitioning to supershear in
718 our model. There is insufficient data from near-field records to confirm this
719 supershear transition of the left propagating rupture. However, if such transi-
720 tion occurred, our model predicts that it is short-lived as the rupture tip
721 gets frustrated by the geometric complexity around the left kink (point E) and
722 slows down to sub-Rayleigh speeds.

723 Furthermore, in some particular cases with large changes to the strike
724 angle a supershear pulse is triggered and forms ahead of the propagating sub-
725 Rayleigh rupture. This behavior captures an interesting feature within the
726 ground motion record in which station 8 (Appendix Figure A1e), located fur-
727 ther along the fault trace than station 7 (Appendix Figure A1f), observes
728 an earlier onset of ground motion. Moreover, the highly segmented nature of
729 the EAF, which is incorporated in our model, contributed to the acceleration
730 and deceleration of the rupture tip at different locations, facilitated dynamic
731 triggering, and enhanced the complexity and intensity of the wavefield which
732 likely increased the damage extent.

733 In addition to the role of geometric complexity, our model reveals that the
734 main rupture tip transitioned to supershear before arriving at Antakya (SW
735 end of the fault trace). This observation is consistent with both the ground
736

motion records revealing dominant FP to FN components within the southern regions, and the extent of ground failures observed within the region.

Furthermore, our numerical analysis suggests that stress and frictional conditions on the fault must have been heterogeneous. This heterogeneity contributed to the continued propagation of the rupture and influenced the rupture speed. Several segments of the fault are also highly stressed due to their orientation with respect to the tectonic stress field. This contributed, for example, to the early supershear transition on the Narli fault and bursts of supershear propagation in the south. A combination of high dynamic stress drop on the Narli fault and a critically stressed EAF around the junction point also facilitated continued propagation. Had the stress field orientation been different by a few degrees, the overall size of the event could have been much smaller.

While previous observations indicate that supershear ruptures are more likely to occur on long fault segments with uniform high stress, on-fault and off-fault heterogeneities can contribute to the emergence of supershear bursts as observed in our dynamic rupture model[43–46]. Furthermore, the geometric complexity may lead to complex wave fields that obscure the Mach cone signature in the far-field. Additional heterogeneity in the velocity structure may also contribute to the masking of the Mach cone in the far-field and makes it harder to detect[47]. However, supershear ruptures have important implications on the local hazard, even if their signature is lost in the far field, due to a combination of factors including (1) a narrow dominant pulse which could cause amplification of shaking for longer period structures, (2) a largely unattenuated shear mach front. Finally, when a rupture transitions from sub-Rayleigh to supershear, there still is a sub-Rayleigh signature following the leading supershear rupture. This is called the trailing Rayleigh signature and propagates at Rayleigh wave speed[13, 22, 48]. As a consequence a building at a near fault location will first experience the intense shaking due to the shock waves of the leading supershear rupture front. This part of the shaking will occur very rapidly (hence the narrow velocity pulse) and is characterized by the fault parallel component of the ground velocity being bigger than the fault normal component[22]. Notice in particular the huge discrepancy in peak velocities between PGV_{FP} and PGV_{FN} (~ 2 times) in station 3129 in Antakya, where the city was truly devastated. However, soon (seconds later) after that, the building will also experience shaking of a different type which is associated with the passage of the trailing Rayleigh rupture. This shaking, features a dominant fault normal component. This double punch effect associated with the first (leading) arrival of the shock front and then the subsequent (trailing) Rayleigh signature can have a devastating impact on the structure. The impact of supershear ruptures on ground and structural failures warrant further investigations.

The role of physics-based dynamic modeling is crucial in our understanding of the mechanism that led to such a devastating outcome. While we cannot at the current time predict the occurrences of earthquakes ahead of time,

783 we may utilize our interpretations to better guide the response during future
784 earthquakes.

785

786 **Methods**

787

788 All numerical simulations were run using an in-house partial differential
789 equation solver built on MOOSE framework[49]. Specifically, we utilize the
790 cohesive zone model capability offered in TensorMechanics system [50] and
791 implement within it a linear slip weakening law [51] as a traction-separation
792 relation that governs the evolution of the dynamic rupture. This nonlinear
793 solver discretizes the governing equations spatially using the finite element
794 method and temporally using explicit time integration via the central difference
795 method.

796

797 **Acknowledgement**

798

799 The ground motion data used in this study can be obtained from Turkish
800 Disaster and Emergency Management Authority AFAD, US Geological Sur-
801 vey (USGS), and Kandilli Observatory And Earthquake Research Institute.
802 We would like to thank the Turkish Disaster and Emergency Management
803 Presidency (AFAD) for setting up dense near-fault observatories, and for
804 immediately publishing a huge number of openly accessible accelerometers
805 during these trying times for Türkiye. A.J.R. acknowledges support by the
806 Caltech/MCE Big Ideas Fund (BIF), as well as the Caltech Terrestrial Hazard
807 Observation and Reporting Center (THOR). He would also like to acknowl-
808 edge the support of NSF (Grant EAR-1651235 and EAR-1651235). A.E.
809 acknowledge support from the Southern California Earthquake Center through
810 a collaborative agreement between NSF. Grant Number: EAR0529922 and
811 USGS. Grant Number: 07HQAG0008 and the National Science Foundation
812 CAREER award No. 1753249 for modeling complex fault zone structures. We
813 are grateful for Idaho National Lab for providing High performance comput-
814 ing support and access and for the MOOSE/Falcon team for offering technical
815 support.

816

817

818

819

820

821

822

823

824

825

826

827

828

Appendix A Full Ground Motion Records

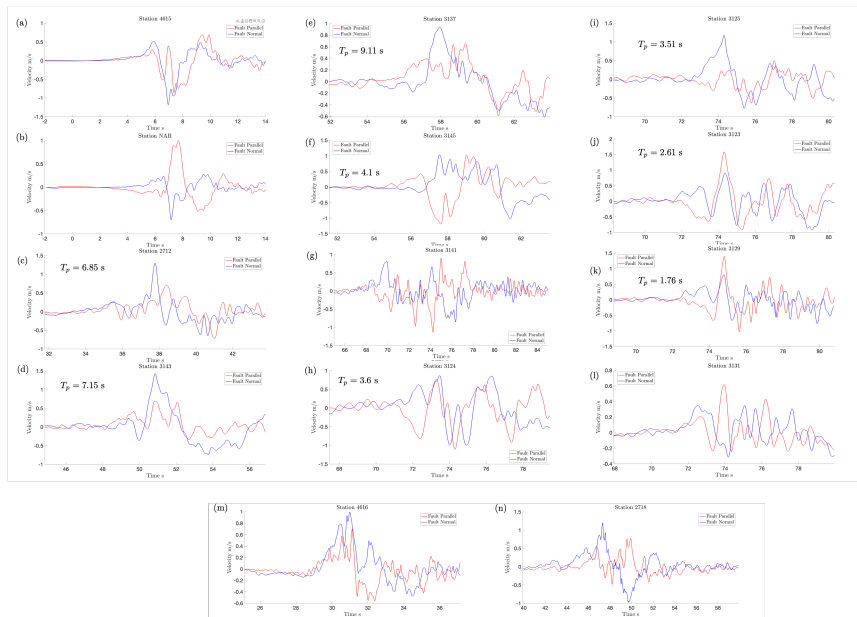


Fig. A1 The instrument corrected records of the fault parallel, and fault normal particle velocities with a 2 second applied filtering for all stations shown in Figure 1 of the manuscript. Within those records we observe three different categories classified based on the ratio of the fault parallel to the fault normal component. (1) A dominant fault normal component suggesting a sub-Rayleigh rupture. (2) A larger fault parallel component relative to the fault normal component suggesting supershear rupture propagation. (3) Comparable fault normal and fault parallel components. The velocity pulse width T_p included in the figures is extracted using methodology presented in Shahi and Baker 2014 [52]. The width of the velocity pulse is narrower for stations showing supershear characteristics.

We note that the ground motion record for station 9 shown in Figure A1g and categorized as probable supershear in Figure 1 show a large degree of complexity beyond the scope of our mechanistic analysis. Initially within the ground motion record we observe a comparable FP to FN components then subsequently we observe large ground motion pulses with primary FP component. Accordingly, we opt to categorize the station as probable supershear. The station complex ground motion record could be attributed to its location in a region with substantial geometrical complexity and multiple fault branches.

Appendix B Stress Calculation

Given maximum principal stress σ_1 and minimum principal stress σ_3 , the normal traction σ_o and tangential traction τ on each fault plane can be evaluated as follows:

829
830
831
832
833
834
835
836
837
838
839
840
841
842
843
844
845
846
847
848
849
850
851
852
853
854
855
856
857
858
859
860
861
862
863
864
865
866
867
868
869
870
871
872
873
874

875
876
877
878
879
880
881
882
883
884
885
886
887
888
889
890
891
892
893
894
895
896
897
898
899
900
901
902
903
904
905
906
907
908
909
910
911
912
913
914
915
916
917
918
919
920

$$\sigma_o = \sigma_1 \sin^2(\theta - \psi) + \sigma_3 \cos^2(\theta - \psi) \quad (\text{B1})$$

$$\tau = (\sigma_1 - \sigma_3) \cos(\theta - \psi) \sin(\theta - \psi) \quad (\text{B2})$$

Where θ is the fault strike, defined as the angle between the fault plane and the north direction, ψ is the angle between the maximum principal stress σ_1 and the north direction. From the above equations, apparent friction μ is expressed as the ratio of shear to normal stress as follows:

$$\mu = \frac{\tau}{\sigma_o} = \frac{(1 - \frac{1}{\frac{\sigma_1}{\sigma_3}}) \cos(\theta - \psi) \sin(\theta - \psi)}{\sin^2(\theta - \psi) + (\frac{1}{\frac{\sigma_1}{\sigma_3}}) \cos^2(\theta - \psi)} \quad (\text{B3})$$

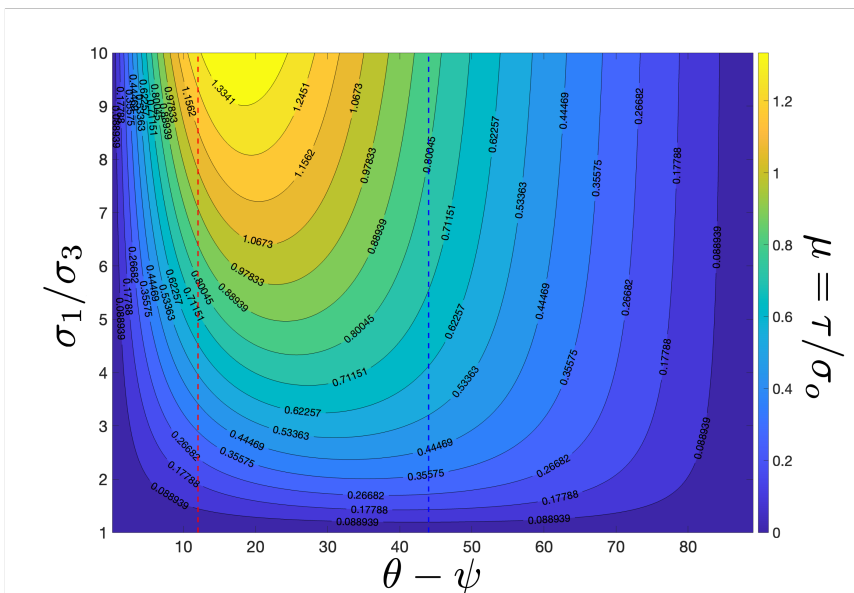


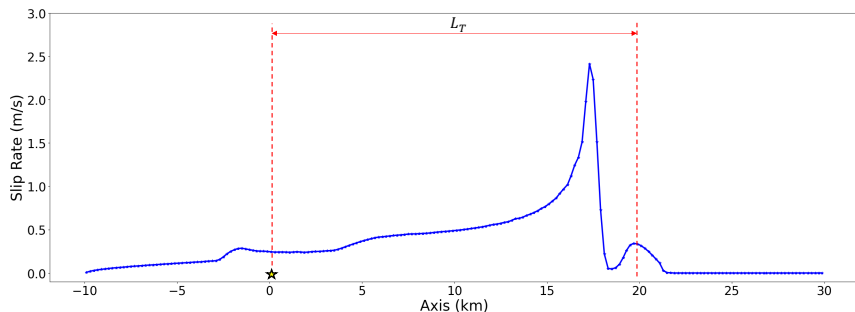
Fig. B2 A contour plot showing the ratio of the resolved shear stress to the normal stress on any fault segment with an arbitrary orientation relative to the maximum principal stress orientation $\theta - \psi$ (the fault strike is θ , which is the angle between the fault plane and the north direction and ψ is the angle between the maximum principal stress σ_1 and the north direction) for different principal stress ratios σ_1/σ_3 . We see that the apparent friction μ is particularly sensitive to the choice of principal stress relative magnitudes. The dashed red and blue lines refer to the specific orientations of the splay fault and the idealized EAF segment around the junction respectively at (12 and 42 degrees).

Appendix C Numerical Discretization

In our dynamic rupture simulations, we discretized the domain using 1.7 million triangle elements with element edge size of 200 m. The choice of

the element size is such that the process zone, which is the fundamental 921
elasto-frictional length scale in our problem, is well resolved. A more detailed 922
discussion for the process zone size for slip-weakening friction law is found in 923
Equations 30a and 33 from Day et. al. 2005 [51]. Day et al. (2005) recommended 924
using 3-5 spatial cells to resolve this critical length scale. This discretization 925
level resolves the critical length scale with 7-8 elements. Temporally, we have 926
used an explicit central difference time integration with time step controlled 927
by the CFL condition. Specifically, the time step in the dynamic rupture sim- 928
ulations corresponds to half the CFL bound: $\Delta t = 0.5\Delta t_{CFL} = 0.5\Delta x/C_p$, 929
where C_p is the dilatational (pressure) wave speed in the solid crust, which is 930
equal to 6000 m/s. We use absorbing boundary conditions at the edges of the 931
simulation domain to enable waves to exit with minimum reflection. 932
933
934
935
936
937
938
939
940
941
942
943
944
945
946
947
948
949
950
951
952
953
954
955
956
957
958
959
960
961
962
963
964
965
966

967 Appendix D Supershear Transition on Narli 968 Fault 969 970



981 **Fig. D3** A snapshot of the slip rate profile on the splay (Narli) fault around
982 the time of transitioning from subRayleigh to supershear propagation. The star
983 represents the hypocenter or the event. The bump at approximately 20km away from the
984 star is the supershear velocity pulse that forms ahead of the trailing sub-Rayleigh crack. The
985 transition length, L_T , which is the distance between the hypocenter and the supershear pulse
986 is shown tentatively on the figure. We used an iterative process to find the dynamic friction
987 coefficient on the splay fault which would result in this specific L_T value that matches what
988 we inferred from the analysis of near-field ground motion records on the Narli fault. See main
989 text for more details.

989
990
991
992
993
994
995
996
997
998
999
1000
1001
1002
1003
1004
1005
1006
1007
1008
1009
1010
1011
1012

Appendix E Peak Slip Rate Spatial Distribution

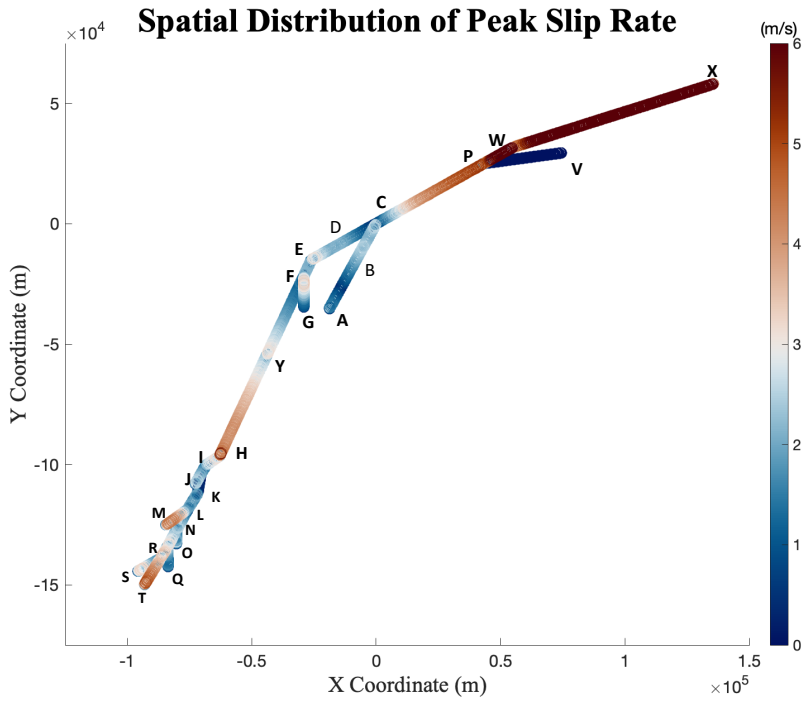


Fig. E4 Peak Slip Rate Spatial Distribution. The 2D scatter plot shows maximum slip rate across the time history along fault paths in the numerical model.

1013
1014
1015
1016
1017
1018
1019
1020
1021
1022
1023
1024
1025
1026
1027
1028
1029
1030
1031
1032
1033
1034
1035
1036
1037
1038
1039
1040
1041
1042
1043
1044
1045
1046
1047
1048
1049
1050
1051
1052
1053
1054
1055
1056
1057
1058

Appendix F Frictional Parameters for Fault Segments

Table F1 Stress and frictional parameters on different fault segments. For the angle with respect to maximum principal stress σ_1 , counter-clockwise direction is assumed positive. For the initial shear stress, the negative value signifies a left lateral shear while a positive value indicates a right lateral shear. The negative initial normal stress represents compression.

Segment Index	Angle with σ_1 (Degree)	Initial Shear Stress τ (MPa)	Initial Normal Stress σ_o (MPa)	Apparent Friction μ	Static Friction μ_s	Dynamic Friction μ_d	Characteristic Length D_c (m)
RT	14.521	-10.922	-17.829	0.613	0.7	0.26	0.392
RS	43.784	-22.48	-36.545	0.615	0.7	0.26	0.803
UR	14.455	-10.878	-17.804	0.611	0.7	0.26	0.391
UQ	-17.292	12.771	-18.976	0.673	0.7	0.26	0.417
NU	11.472	-8.771	-16.78	0.523	0.7	0.26	0.369
NO	-14.971	11.231	-18.003	0.624	0.7	0.26	0.396
LN	11.585	-8.853	-16.815	0.526	0.7	0.26	0.369
LM	37.499	-21.733	-31.676	0.686	0.7	0.26	0.696
KL	14.717	-11.057	-17.904	0.618	0.7	0.26	0.393
IK	-7.567	5.874	-15.78	0.372	0.7	0.26	0.347
IJ	12.531	-9.531	-17.118	0.557	0.7	0.26	0.376
IH	38.169	-21.863	-32.186	0.679	0.7	0.26	0.707
YH	8.352	-6.467	-15.949	0.405	0.7	0.26	0.35
FY	8.36	-6.473	-15.951	0.406	0.7	0.26	0.35
FG	-15.64	11.682	-18.271	0.639	0.7	0.26	0.401
EF	8.36	-6.473	-15.951	0.406	0.7	0.26	0.35
CE	44	-22.486	-36.715	0.612	0.7	0.515	0.339
AC	12	-9.152	-16.945	0.54	0.7	0.327	0.316
CP	44	-22.486	-36.715	0.612	0.7	0.515	0.339
PV	66.027	-16.706	-52.571	0.318	0.7	0.3	1.05
PW	44.025	-22.487	-36.735	0.612	0.7	0.3	0.734
WX	55.91	-20.888	-45.863	0.455	0.7	0.3	0.916

References

- 1105
1106
1107
1108
1109
1110
1111
1112
1113
1114
1115
1116
1117
1118
1119
1120
1121
1122
1123
1124
1125
1126
1127
1128
1129
1130
1131
1132
1133
1134
1135
1136
1137
1138
1139
1140
1141
1142
1143
1144
1145
1146
1147
1148
1149
1150
- [1] US Geological Survey: M 7.8 - 27 km E of Nurdağı, Turkey. <https://earthquake.usgs.gov/earthquakes/eventpage/us6000jllz/executive>
- [2] Disaster, Authority, E.M.: Turkish National Strong Motion Network. Department of Earthquake, Disaster and Emergency Management Authority (1973). <https://doi.org/10.7914/SN/TK>. <https://tadas.afad.gov.tr>
- [3] Dal Zilio, L., Ampuero, J.-P.: Earthquake doublet in Turkey and Syria. *Communications Earth & Environment* **4**(1), 71 (2023). <https://doi.org/10.1038/s43247-023-00747-z>
- [4] Feyiz Kartal, R., Tuba Kadirioglu, F.: Kinematic of East Anatolian Fault and Dead Sea Fault. Technical report (2013). <https://www.researchgate.net/publication/271852091>
- [5] Ambraseys, N.N.: Temporary seismic quiescence: SE Turkey. Technical report (1989). <https://academic.oup.com/gji/article/96/2/311/611031>
- [6] Ambraseys, N.N., Jackson, J.A.: Seismicity of the Sea of Marmara (Turkey) since 1500. *Geophysical Journal International* **141**(3) (2000). <https://doi.org/10.1046/j.1365-246X.2000.00137.x>
- [7] Poliakov, A.N.B., Dmowska, R., Rice, J.R.: Dynamic shear rupture interactions with fault bends and off-axis secondary faulting. *Journal of Geophysical Research: Solid Earth* **107**(B11), 6–1 (2002). <https://doi.org/10.1029/2001jb000572>
- [8] Bhat, H.S., Olives, M., Dmowska, R., Rice, J.R.: Role of fault branches in earthquake rupture dynamics. *Journal of Geophysical Research: Solid Earth* **112**(11) (2007). <https://doi.org/10.1029/2007JB005027>
- [9] Ma, X., Elbanna, A.: Dynamic rupture propagation on fault planes with explicit representation of short branches. *Earth and Planetary Science Letters* **523**, 115702 (2019). <https://doi.org/10.1016/j.epsl.2019.07.005>
- [10] Biegel, R.L., Sammis, C.G., Rosakis, A.J.: Interaction of a dynamic rupture on a fault plane with short frictionless fault branches. *Pure and Applied Geophysics* **164**(10), 1881–1904 (2007). <https://doi.org/10.1007/s00024-007-0251-2>
- [11] Bhat, H.S., Dmowska, R., Rice, J.R., Kame, N.: Dynamic Slip Transfer from the Denali to Totschunda Faults, Alaska: Testing Theory for Fault Branching. Technical Report 6B (2004). http://pubs.geoscienceworld.org/ssa/bssa/article-pdf/94/6B/S202/2720488/S202_946b_04601.pdf

- 1151 [12] Rosakis, A., Abdelmeguid, M., Elbanna, A.: Evidence of Early Supershear
 1152 Transition in the M_w 7.8 Kahramanmaraş Earthquake From Near-Field
 1153 Records. <https://doi.org/10.31223/X5W95G>
 1154
- 1155 [13] Dunham, E.M., Bhat, H.S.: Attenuation of radiated ground motion and
 1156 stresses from three-dimensional supershear ruptures. *Journal of Geophys-*
 1157 *ical Research: Solid Earth* **113**(B8), 1–17 (2008). [https://doi.org/10.1029/](https://doi.org/10.1029/2007JB005182)
 1158 [2007JB005182](https://doi.org/10.1029/2007JB005182)
- 1159 [14] Harris, R.A., Day, S.M.: Dynamics of fault interaction: parallel strike-
 1160 slip faults. *Journal of Geophysical Research* **98**(B3), 4461–4472 (1993).
 1161 <https://doi.org/10.1029/92JB02272>
 1162
- 1163 [15] Melgar, D., Taymaz, T., Ganas, A., Crowell, B., Öcalan, T., Kahraman,
 1164 M., Tsironi, V., Yolsal-Çevikbil, S., Valkaniotis, S., Irmak, T.S., Eken,
 1165 T., Erman, C., Özkan, B., Dogan, A.H., Altuntaş, C.: Sub- and super-
 1166 shear ruptures during the 2023 M_w 7.8 and M_w 7.6 earthquake doublet
 1167 in SE Türkiye. *Seismica* **2**(3) (2023). [https://doi.org/10.26443/seismica.](https://doi.org/10.26443/seismica.v2i3.387)
 1168 [v2i3.387](https://doi.org/10.26443/seismica.v2i3.387)
 1169
- 1170 [16] Oglesby, D.D., Mai, P.M.: Fault geometry, rupture dynamics and ground
 1171 motion from potential earthquakes on the North Anatolian Fault under
 1172 the Sea of Marmara. *Geophysical Journal International* **188**(3), 1071–1087
 1173 (2012). <https://doi.org/10.1111/j.1365-246X.2011.05289.x>
 1174
- 1175 [17] Zahradnik, J., Turhan, F., Sokos, E., Gallovič, F.: Asperity-like (seg-
 1176 mented) structure of the 6 february 2023 turkish earthquakes (2023).
 1177 <https://doi.org/10.31223/X5T666>
 1178
- 1179 [18] Okuwaki, R., Yagi, Y., Taymaz, T., Hicks, S.: Multi-scale rupture growth
 1180 with alternating directions in a complex fault network during the 2023
 1181 south-eastern türkiye and syria earthquake doublet (2023). [https://doi.](https://doi.org/10.31223/X5RD4W)
 1182 [org/10.31223/X5RD4W](https://doi.org/10.31223/X5RD4W)
 1183
- 1184 [19] Kandilli Observatory And Earthquake Research Institute Boğaziçi
 1185 University: Kandilli Observatory And Earthquake Research Insti-
 1186 tute (KOERI). International Federation of Digital Seismograph Net-
 1187 works (1971). <https://doi.org/10.7914/SN/KO>. [https://www.fdsn.org/](https://www.fdsn.org/networks/detail/KO/)
 1188 [networks/detail/KO/](https://www.fdsn.org/networks/detail/KO/)
 1189
- 1190 [20] Rosakis, A.J., Samudrala, O., Coker, D.: Cracks Faster than the Shear
 1191 Wave Speed. *Science* **284**(5418), 1337–1340 (1999). [https://doi.org/10.](https://doi.org/10.1126/science.284.5418.1337)
 1192 [1126/science.284.5418.1337](https://doi.org/10.1126/science.284.5418.1337)
 1193
- 1194 [21] Bouchon, M., Karabulut, H., Bouin, M.P., Schmittbuhl, J., Vallée, M.,
 1195 Archuleta, R., Das, S., Renard, F., Marsan, D.: Faulting characteristics of
 1196 supershear earthquakes. *Tectonophysics* **493**(3-4), 244–253 (2010). <https://doi.org/10.1016/j.tecto.2010.07.011>

- [//doi.org/10.1016/j.tecto.2010.06.011](https://doi.org/10.1016/j.tecto.2010.06.011) 1197
1198
- [22] Mello, M., Bhat, H.S., Rosakis, A.J.: Spatiotemporal properties of Sub-Rayleigh and supershear rupture velocity fields: Theory and experiments. *Journal of the Mechanics and Physics of Solids* **93**, 153–181 (2016). <https://doi.org/10.1016/j.jmps.2016.02.031> 1199
1200
1201
1202
1203
- [23] Rubino, V., Rosakis, A.J., Lapusta, N.: Spatiotemporal Properties of Sub-Rayleigh and Supershear Ruptures Inferred From Full-Field Dynamic Imaging of Laboratory Experiments. *Journal of Geophysical Research: Solid Earth* **125**(2) (2020). <https://doi.org/10.1029/2019JB018922> 1204
1205
1206
1207
1208
- [24] Acarel, D., Cambaz, M.D., Turhan, F., Mutlu, A.K., Polat, R.: Seis-motectonics of Malatya Fault, Eastern Turkey. *Open Geosciences* **11**(1), 1098–1111 (2019). <https://doi.org/10.1515/geo-2019-0085> 1209
1210
1211
- [25] Lockner, D.A., Byerlee, J.D., Kuksenkot, V., Ponomarev, A., Sidorin, A.: Quasi-static fault growth and shear fracture energy in granite. Technical report (1991) 1212
1213
1214
1215
- [26] Lockner, D.A., Byerlee, J.D., Kuksenko, V., Ponomarev, A., Sidorin, A.: Chapter 1 Observations of Quasistatic Fault Growth from Acoustic Emissions. In: Evans, B., Wong, T.-f. (eds.) *Fault Mechanics and Transport Properties of Rocks*. International Geophysics, vol. 51, pp. 3–31. Academic Press, ??? (1992). [https://doi.org/10.1016/S0074-6142\(08\)62813-2](https://doi.org/10.1016/S0074-6142(08)62813-2). <https://www.sciencedirect.com/science/article/pii/S0074614208628132> 1216
1217
1218
1219
1220
1221
1222
- [27] Palmer, A.C., Rice, J.R.: The growth of slip surfaces in the progressive failure of over-consolidated clay. *Proceedings of the Royal Society of London. A. Mathematical and Physical Sciences* **332**(1591), 527–548 (1973). <https://doi.org/10.1098/rspa.1973.0040> 1223
1224
1225
1226
1227
- [28] Ida, Y.: Cohesive force across the tip of a longitudinal-shear crack and Griffith’s specific surface energy. *Journal of Geophysical Research* **77**(20), 3796–3805 (1972). <https://doi.org/10.1029/jb077i020p03796> 1228
1229
1230
- [29] Andrews, D.J.: Rupture Velocity of Plane Strain Shear Cracks. *J Geophys Res* **81**(32), 5679–5687 (1976). <https://doi.org/10.1029/JB081i032p05679> 1231
1232
1233
1234
- [30] Das, S., Aki, K.: A numerical study of two-dimensional spontaneous rupture propagation. *Geophysical Journal International* **50**(3), 643–668 (1977). <https://doi.org/10.1111/j.1365-246X.1977.tb01339.x> 1235
1236
1237
1238
- [31] Dunham, E.M.: Conditions governing the occurrence of supershear ruptures under slip-weakening friction. *Journal of Geophysical Research* **112**(B7), 07302 (2007). <https://doi.org/10.1029/2006JB004717> 1239
1240
1241
1242

- 1243 [32] Abercrombie, R.E., Rice, J.R.: Can observations of earthquake scaling
 1244 constrain slip weakening? (2005). [https://doi.org/10.1111/j.1365-246X.](https://doi.org/10.1111/j.1365-246X.2005.02579.x)
 1245 [2005.02579.x](https://doi.org/10.1111/j.1365-246X.2005.02579.x)
 1246
- 1247 [33] Byerlee, J.: Friction of rocks. *pure and applied geophysics* **116**(4), 615–626
 1248 (1978). <https://doi.org/10.1007/BF00876528>
 1249
- 1250 [34] Fialko, Y., Jin, Z.: Simple shear origin of the cross-faults ruptured in the
 1251 2019 Ridgecrest earthquake sequence. *Nature Geoscience* **14**(7), 513–518
 1252 (2021). <https://doi.org/10.1038/s41561-021-00758-5>
 1253
- 1254 [35] Rousseau, C.-E., Rosakis, A.J.: On the influence of fault bends on the
 1255 growth of sub-Rayleigh and intersonic dynamic shear ruptures. *Journal*
 1256 *of Geophysical Research: Solid Earth* **108**(B9) (2003). [https://doi.org/10.](https://doi.org/10.1029/2002jb002310)
 1257 [1029/2002jb002310](https://doi.org/10.1029/2002jb002310)
- 1258 [36] Rousseau, C.E., Rosakis, A.J.: Dynamic path selection along branched
 1259 faults: Experiments involving sub-Rayleigh and supershear ruptures.
 1260 *Journal of Geophysical Research: Solid Earth* **114**(8), 1–15 (2009). [https:](https://doi.org/10.1029/2008JB006173)
 1261 [//doi.org/10.1029/2008JB006173](https://doi.org/10.1029/2008JB006173)
 1262
- 1263 [37] Güvercin, S.E., Karabulut, H., Konca, A., Doğan, U., Ergintav, S.:
 1264 Active seismotectonics of the East Anatolian Fault. *Geophysical Journal*
 1265 *International* **230**(1), 50–69 (2022). <https://doi.org/10.1093/gji/ggac045>
 1266
- 1267 [38] Bulut, F., Bohnhoff, M., Eken, T., Janssen, C., Kl, T., Dresen, G.: The
 1268 East Anatolian Fault Zone: Seismotectonic setting and spatiotemporal
 1269 characteristics of seismicity based on precise earthquake locations. *Journal*
 1270 *of Geophysical Research: Solid Earth* **117**(7) (2012). [https://doi.org/10.](https://doi.org/10.1029/2011JB008966)
 1271 [1029/2011JB008966](https://doi.org/10.1029/2011JB008966)
 1272
- 1273 [39] Şengör, A.M.C., Görür, N., Şaroğlu, F.: Strike-Slip Faulting and
 1274 Related Basin Formation in Zones of Tectonic Escape: Turkey as
 1275 a Case Study. In: *Strike-Slip Deformation, Basin Formation, and*
 1276 *Sedimentation*, pp. 211–226. SEPM (Society for Sedimentary Geol-
 1277 ogy), ??? (1985). <https://doi.org/10.2110/pec.85.37.0211>. [https://pubs.](https://pubs.geoscienceworld.org/books/book/1091/chapter/10548841/)
 1278 [geoscienceworld.org/books/book/1091/chapter/10548841/](https://pubs.geoscienceworld.org/books/book/1091/chapter/10548841/)
 1279
- 1280 [40] Taftoglou, M., Valkaniotis, S., Karantanellis, E., Goula, E., Papathanasiou, G.: Preliminary mapping of liquefaction phenomena triggered by the february 6 2023 m7.7 earthquake, türkiye / syria, based on remote sensing data (2023). <https://doi.org/10.5281/zenodo.7668401>
 1281
 1282
 1283
- 1284 [41] Templeton, E.L., Baudet, A., Bhat, H.S., Dmowska, R., Rice, J.R.,
 1285 Rosakis, A.J., Rousseau, C.E.: Finite element simulations of dynamic
 1286 shear rupture experiments and dynamic path selection along kinked and
 1287 branched faults. *Journal of Geophysical Research: Solid Earth* **114**(8)
 1288

- (2009). <https://doi.org/10.1029/2008JB006174> 1289
1290
- [42] Rousseau, C.E., Rosakis, A.J.: Dynamic path selection along branched faults: Experiments involving sub-Rayleigh and supershear ruptures. *Journal of Geophysical Research: Solid Earth* **114**(8), 1–15 (2009). <https://doi.org/10.1029/2008JB006173> 1291
1292
1293
1294
1295
- [43] Dunham, E.M., Favreau, P., Carlson, J.M.: A Supershear Transition Mechanism for Cracks. *Science* **299**(5612), 1557–1559 (2003). <https://doi.org/10.1126/science.1080650> 1296
1297
1298
1299
- [44] Liu, Y., Lapusta, N.: Transition of mode II cracks from sub-Rayleigh to intersonic speeds in the presence of favorable heterogeneity. *Journal of the Mechanics and Physics of Solids* **56**(1), 25–50 (2008). <https://doi.org/10.1016/j.jmps.2007.06.005> 1300
1301
1302
1303
- [45] Ma, X., Elbanna, A.E.: Effect of off-fault low-velocity elastic inclusions on supershear rupture dynamics. *Geophysical Journal International* **203**(1), 664–677 (2015). <https://doi.org/10.1093/gji/ggv302> 1304
1305
1306
1307
- [46] Bruhat, L., Fang, Z., Dunham, E.M.: Rupture complexity and the supershear transition on rough faults. *Journal of Geophysical Research: Solid Earth* **121**, 210–224 (2016). <https://doi.org/10.1002/2015JB012512> 1308
1309
1310
1311
- [47] Bizzarri, A., Dunham, E.M., Spudich, P.: Coherence of mach fronts during heterogeneous supershear earthquake rupture propagation: Simulations and comparison with observations. *Journal of Geophysical Research: Solid Earth* **115** (2010). <https://doi.org/10.1029/2009JB006819> 1312
1313
1314
1315
1316
- [48] Mello, M., Bhat, H.S., Rosakis, A.J., Kanamori, H.: Reproducing the supershear portion of the 2002 Denali earthquake rupture in laboratory. *Earth and Planetary Science Letters* **387**, 89–96 (2014). <https://doi.org/10.1016/j.epsl.2013.11.030> 1317
1318
1319
1320
1321
- [49] Lindsay, A.D., Gaston, D.R., Permann, C.J., Miller, J.M., Andrš, D., Slaughter, A.E., Kong, F., Hansel, J., Carlsen, R.W., Icenhour, C., Harbour, L., Giudicelli, G.L., Stogner, R.H., German, P., Badger, J., Biswas, S., Chapuis, L., Green, C., Hales, J., Hu, T., Jiang, W., Jung, Y.S., Matthews, C., Miao, Y., Novak, A., Peterson, J.W., Prince, Z.M., Rovinelli, A., Schunert, S., Schwen, D., Spencer, B.W., Veeraraghavan, S., Recuero, A., Yushu, D., Wang, Y., Wilkins, A., Wong, C.: 2.0 - MOOSE: Enabling massively parallel multiphysics simulation. *SoftwareX* **20**, 101202 (2022). <https://doi.org/10.1016/j.softx.2022.101202> 1322
1323
1324
1325
1326
1327
1328
1329
1330
- [50] Adhikary, D.P., Jayasundara, C., Podgorney, R.K., Wilkins, A.H.: A robust return-map algorithm for general multisurface plasticity. *International Journal for Numerical Methods in Engineering* **109**, 218–234 1331
1332
1333
1334

1335 (2016). <https://doi.org/10.1002/nme.5284>

1336

1337 [51] Day, S.M., Dalguer, L.A., Lapusta, N., Liu, Y.: Comparison of finite
1338 difference and boundary integral solutions to three-dimensional sponta-
1339 neous rupture. *Journal of Geophysical Research: Solid Earth* **110**(12),
1340 1–23 (2005). <https://doi.org/10.1029/2005JB003813>

1341

1342 [52] Shahi, S.K., Baker, J.W.: An efficient algorithm to identify strong-velocity
1343 pulses in multicomponent ground motions. *Bulletin of the Seismologi-
1344 cal Society of America* **104**, 2456–2466 (2014). [https://doi.org/10.1785/
1345 0120130191](https://doi.org/10.1785/0120130191)

1346

1347

1348

1349

1350

1351

1352

1353

1354

1355

1356

1357

1358

1359

1360

1361

1362

1363

1364

1365

1366

1367

1368

1369

1370

1371

1372

1373

1374

1375

1376

1377

1378

1379

1380